Scripta Materialia 208 (2022) 114344

Contents lists available at ScienceDirect

Scripta Materialia

journal homepage: www.elsevier.com/locate/scriptamat

Helium partitioning to the core-shelled Ta nanoclusters in nanocrystalline Cu-Ta alloy

S. Srinivasan[a], B.C. Hornbuckle[b], K.A. Darling[b], H. Kim[c], Y.Q. Wang[c], K. Solanki[a,*]

[a] School for the Engineering of Matter, Transport, and Energy, Arizona State University, Tempe, AZ, 85287, USA
[b] US CCDC Army Research Laboratory, Weapons, and Materials Research Directorate, APG, MD, 21005, USA
[c] Materials Science and Technology Division, Los Alamos National Laboratory, Los Alamos, NM, 87545, USA

ARTICLE INFO

Article history:
Received 1 September 2021
Revised 7 October 2021
Accepted 11 October 2021
Available online 21 October 2021

Keywords:
Irradiation
Helium bubbles
Nanocrystalline
Core-shell structure

ABSTRACT

In this work, a nanocrystalline (NC) Cu-10at.%Ta alloy is irradiated with helium at different temperatures to assess the stability and effectiveness of Ta nanoclusters in trapping helium and suppressing swelling. Advanced microstructural characterization of the room-temperature irradiated specimens indicated the presence of small He-bubbles (~1-2 nm) at the peak damage depth mainly at the core and along the interface of Ta nanoclusters with Cu matrix. Few bubbles were found along grain boundaries, with much smaller bubbles homogenously distributed within the copper lattice. High-temperature irradiation exhibited bubbles of ~3-5 nm, which were primarily associated with nanoclusters as compared to other locations, with no observed faceting of the bubbles. Atom probe analysis confirmed helium partitioning to the Ta nanoclusters indicating the effective entrapment of these He atoms.

Efficient operation and extended lifetime of future nuclear reactors depend on the performance of structural materials in extreme radiation environments [1]. High energy particle radiation causes displacement of atoms from their lattice sites resulting in the formation of numerous point defects (vacancies and interstitials) whose subsequent diffusion and clustering lead to volumetric swelling, hardening, phase segregation, disordering, etc., in reactor structural materials [2]. Particularly, helium generated by nuclear transmutation (n, α) reactions is more detrimental in advanced fast reactors and fusion devices as it exacerbates the effects from displacement damage. Due to its low solubility in metals and high binding energy with vacancies, helium tends to exist as helium vacancy complexes, thereby stabilizing the vacancy clusters (from reemission) [3–7]. These defect interactions (low migration energy of helium) and complex microstructural evolutions (with temperature, dose, dose rate, He concentration), ranging from small helium bubbles to large faceted voids can aggravate the radiation-induced degradation such as void swelling and helium embrittlement [8]. Various promising strategies have been proposed to alleviate such radiation effects through nano-engineering of a high density of planar and linear microstructural defects including grain boundaries (GBs), phase boundaries, and dislocations that act as effective interface sinks for the radiation-induced defects [9]. For instance, experimental evidence has shown that refining grain size down to the nano regime can improve radiation tolerance [10], provided the microstructure is stable under a relevant radiation environment. Likewise, many studies have reported enhanced radiation resistance in ODS and NFA (Nanostructured Ferritic alloys) compared to conventional austenitic alloys [11,12]. Metallic nanolayers are another attractive group of materials widely researched for their effective suppression of radiation-induced defects and helium bubble swelling owing to numerous heterophase interfaces [13,14]. Furthermore, immiscible and semi-coherent (e.g., fcc/bcc) interfaces have been proclaimed to offer promising radiation tolerance compared to their miscible (e.g., Al/Nb, Fe/W) and coherent (e.g., fcc/fcc: Ag/Ni) counterparts due to the presence of large free volume for the absorption of defects [15–18]. The motivation of this study is to understand the cumulative defect trapping efficiency and stability of immiscible interfaces and nanocrystalline GBs decorated with nano precipitates in a binary alloy system to helium irradiation. One such immiscible system: bulk Cu-10at.%Ta [19–21], with nanocrystalline (NC) microstructure and bimodal distribution of precipitates (nanoclusters and large particles) has shown promising radiation tolerance to high dose heavy ion irradiation [22]. Thus, in this study, we use this nanocrystalline Cu-Ta alloy (NC-Cu-10at.% Ta) with numerous immiscible interfaces, to evaluate the stability and tolerance of such a system to high helium concentrations and temperature.

Towards this, NC-Cu-Ta cylindrical specimens with 3 mm diameter and ~1.2 mm tall, were mechanically polished to a mirror finish and irradiated with 200 keV He^{++} ions on Danfysik Ion Im-

* Corresponding author.
E-mail address: kiran.solanki@asu.edu (K. Solanki).

https://doi.org/10.1016/j.scriptamat.2021.114344
1359-6462/

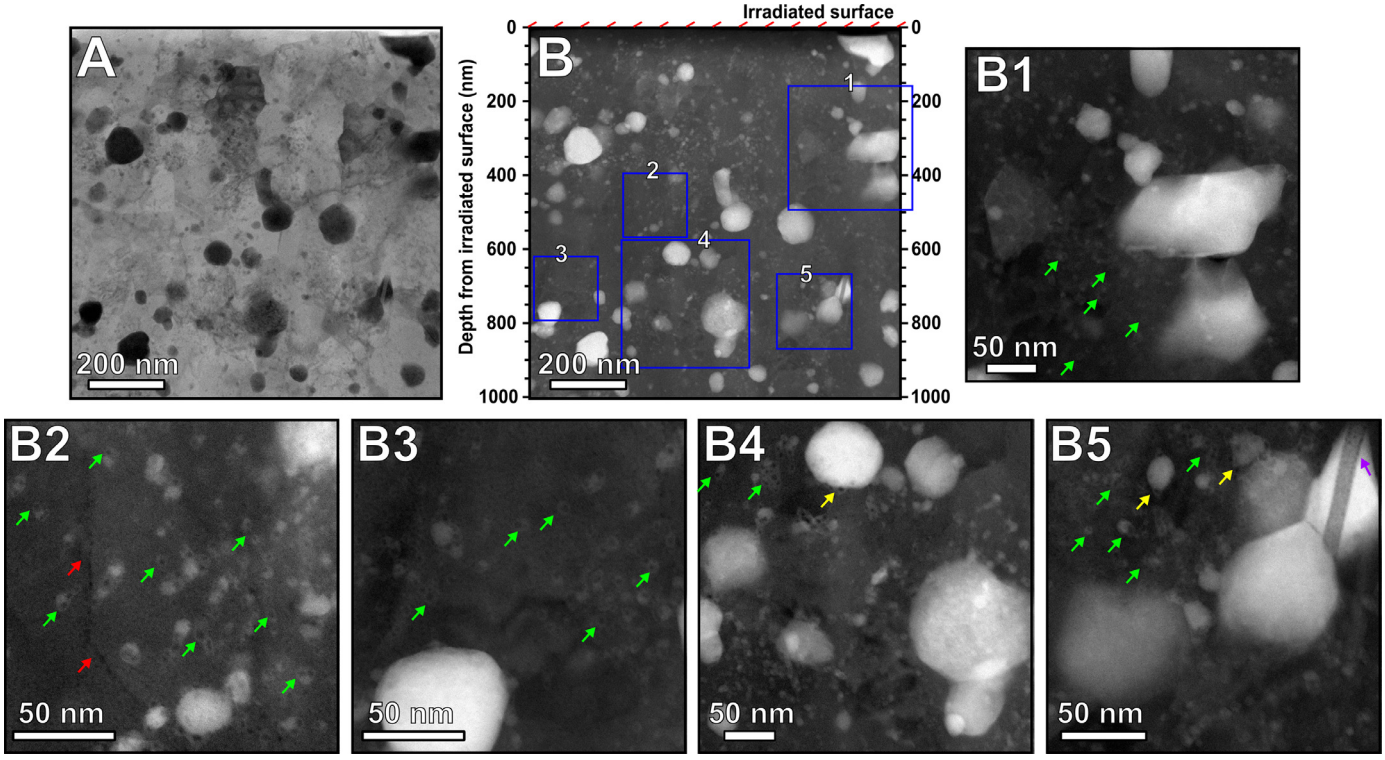

Fig. 1. Helium bubble distribution at RT. (A) Low magnification BF STEM image showing the complete damage region from the irradiated surface. (B) Corresponding HAADF STEM image of A. B1-B5 represents high magnification HAADF image at various irradiation depth in image B showing the bubble distribution. Arrows point to bubbles at various interfaces such as Red-Grain boundaries, Yellow-Large Ta interfaces, and Green-Ta nanoclusters.

planter at Ion Beam Materials Laboratory in Los Alamos National Laboratory. The beam was raster-scanned with a frequency of ~1.1 kHz in x and y. A flux of 1.85×10^{13} ions cm^{-2} s^{-1} was used to achieve a fluence of 1×10^{17} ions cm^{-2} at room temperature (RT) and 723 K. The samples were mounted to the heating stage with silver paste for good thermal conduction, and the stage temperature was monitored through a thermocouple attached to the stage. Damage profiles were calculated using Stopping and Range of Ions in Matter (SRIM) software utilizing the Kinchin Pease model, which gives the best correlation with the internationally adopted Norgett, Robinson, and Torrens (NRT) displacement model [23]. The simulation was performed for Cu-10at.%Ta with threshold displacement energy of copper and tantalum set to 30 eV and 90 eV respectively [24]. Damage profiles in displacements per atom (dpa, **Figure S1**), indicate a damage level of 0.5 dpa near the surface (relatively flat), with peak damage of 2.5 dpa occurring at 0.5 µm and peak helium concentration of 4 at.% at 0.7 µm. For transmission electron microscopy (TEM) characterization was carried out in an ARM-200F, samples were prepared using a Focused Ion beam (FIB) FEI Nova 500 to get cross-section liftouts of the irradiated region which were thinned to electron transparency till 2 keV and were plasma cleaned in Ar prior to TEM observations to reduce FIB damage and surface contamination. More than 150 grains were sampled using ImageJ software to get the average grain size from the irradiated depth spanning from 100-600 nm. Bubble statistics were determined with the help of HAADF (High Annular Angular Dark Field) images. Swelling analysis was carried out over different depths, quantifying bubble size and density using ImageJ software. Atom probe tomography was performed using a Cameca LEAP 5000 XR system operated at 50 K with laser energy of 50 pJ, auto pulse rate control enabled with a minimum mass spectrum range of 300 Dalton, and target evaporation rate of 0.5%. The atom probe samples were prepared with a ThermoFisher Scientific Helios G4 UX dual-beam focused ion beam (FIB) / scanning electron microscope (SEM). Annular milling was utilized to yield the appropriate needle-shaped geometry to facilitate field evaporation. The final step in the annular milling process was conducted at 5 keV to minimize Ga implantation into the tip. After running the tip, the reconstruction and analysis were performed using IVAS 3.8.4 software. All analyzed tips were composed of at least 20 million ions.

Post irradiation microstructure of the RT implanted specimen was analyzed at different irradiation depths as shown in Fig. 1. Tiny helium bubbles of ~1-2 nm began to be observed along the Ta nanoclusters at the irradiation depth of around 300 nm (i.e., ~0.5 at.% He), below which bubbles were difficult to be detected. No bubbles were observed elsewhere until 400 nm. As the irradiation depth approached the peak damage region at >400 nm, in addition to more bubbles being associated with the nanoclusters, minute bubbles of < 1 nm were observed to be uniformly distributed in the matrix as seen from the HAADF images in Fig. 1 (B2 and B3). Furthermore, bubbles of ~ 2 nm were observed along a few GBs (Fig. 2 B2) and some larger Ta precipitate interfaces as well (Fig. 2 B4). Nevertheless, the bubbles at these GBs remained small (~2 nm) potentially due to the sequestering effect from tantalum nanoclusters present at the GBs, increasing the threshold for coalescence. A considerable fraction of bubbles (~2-3 nm) was observed at the nanoclusters and interestingly more along the defected core of the core-shell structure exhibited by these nanoclusters in addition to their interfaces.

Similar microstructure analysis was carried out at various irradiation depths for the specimen irradiated at 723 K as shown in Fig. 2. No bubbles could be detected below ~180-200 nm, indicating a critical helium concentration of ~0.17 - 0.2 at.% He required for bubbles to nucleate. In other words, critical helium concentration per interface area in Cu-Ta is ~7.8-9.9 atoms/nm^2. At depths ranging from 200-400 nm (i.e., 0.2- 1 at.% He), small bubbles of 2-3 nm were observed primarily along the Ta nanoclusters and a few

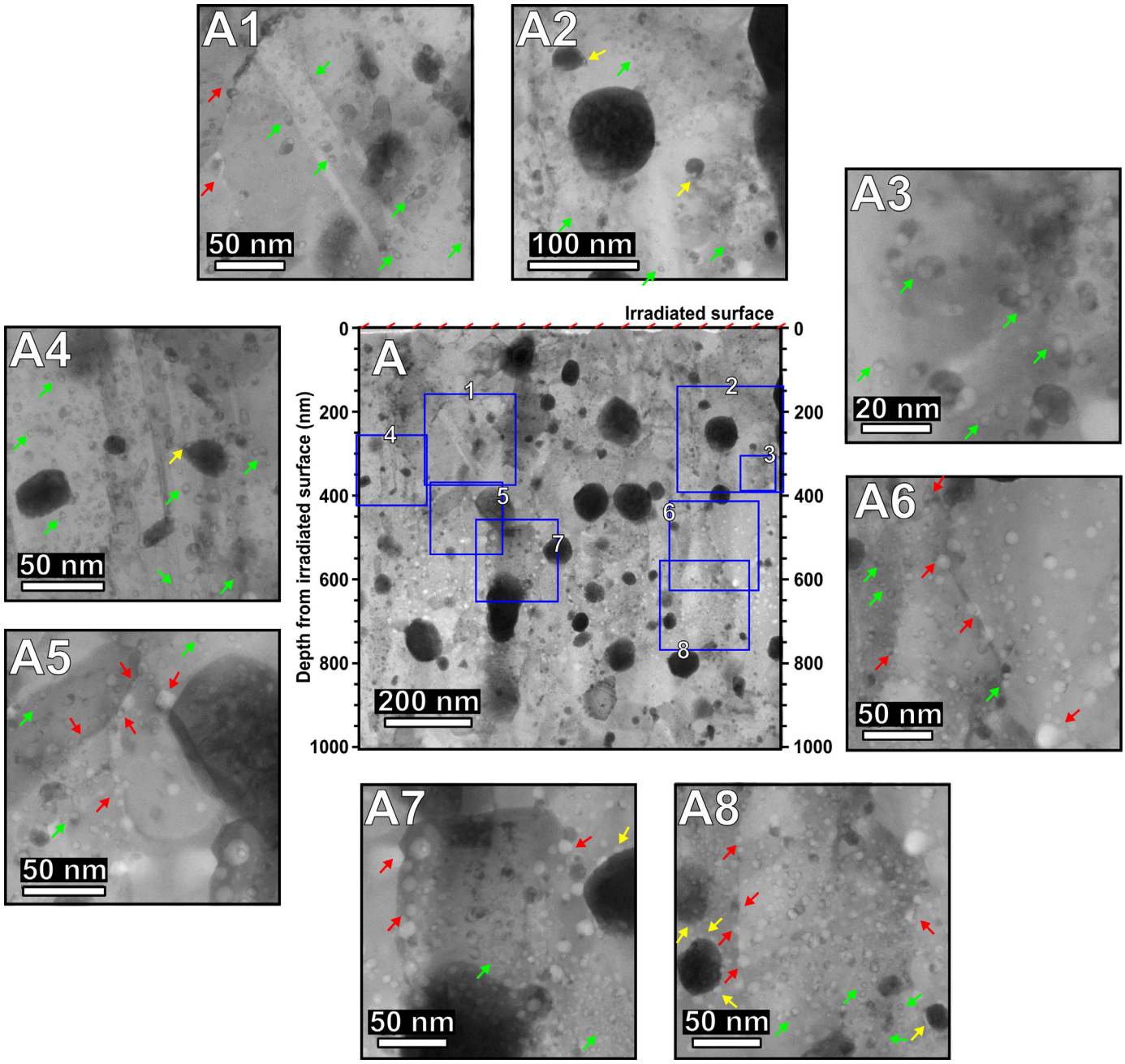

Fig. 2. Helium bubble distribution at 723 K. (A) Low magnification BF STEM image showing the complete damage region from the irradiated surface. A1-A8 are high magnification images at various irradiation depths in image A. Arrows point to bubbles at various interfaces such as Red-Grain boundaries, Yellow- Large Ta interfaces, and Green- Ta nanoclusters.

GBs indicating the preference of helium bubbles to segregate to these interfaces before aggregating at the matrix or GBs. No bubbles were observed in the bulk (within the grains). As the dose increased drastically approaching the peak damage region at depths >400 nm (i.e., 1 to 4 at.% He), bubbles of average size 4-5 nm were observed both along the GBs (Fig. 2 A5-6) and within the grains (Fig. 2 A7-8). Moreover, the largest bubble observed at the peak helium concentration was around 10 nm with no evident faceting. Even at the peak helium concentration, many of the bubbles associated with the nanoclusters in both matrix and GBs were observed to remain within the range of 3-4 nm indicating the potential of these clusters in resisting bubble coarsening (Fig. 2 A3&A8). Furthermore, SEM imaging of the irradiated surface showed no prominent blistering for both RT and 723 K conditions.

Quantitative analysis of helium bubble evolution in the 723 K implantation was carried out by plotting the average size and swelling distribution as a function of irradiation depth (dose) as shown in Fig. 3. As seen in Fig. 3B, the average swelling at dose levels of 1 dpa and 0.5 at.% He is as low as 0.05%. As the dose and helium concentration increased, the swelling % increased to an average of ~0.7% at the peak damage region (2.5 dpa and 4 at.% He). In the similar irradiation depth zone (>400 nm), the average bubble size varied between a small range of 2.5 nm to 5 nm, however, there was a significant change in the swelling % indicating the added role of defect number density on the overall swelling behavior. Nevertheless, the observed swelling % at peak helium concentration is comparable/slightly lower than that observed in candidate NFA 14YWT and Cu-V nanolayers at a similar dose and

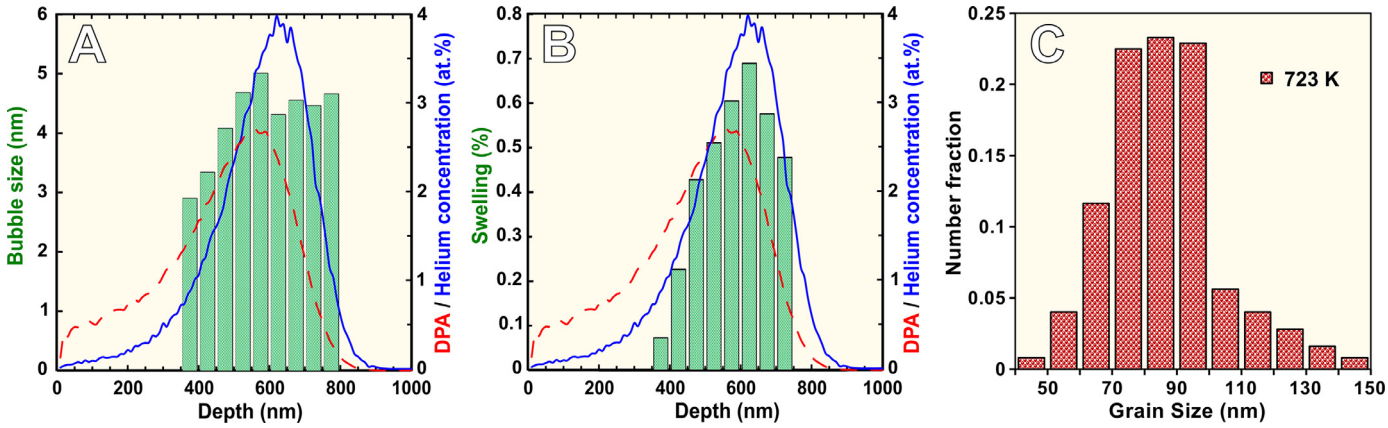

Fig. 3. Helium bubble and grain statistics at 723 K. (A) Bubble size distribution as a function of irradiation depth (dose). (B) Calculated swelling % along the irradiation depth. (C) Grain size distribution of the sample irradiated at 723 K obtained from the depth span of 100-600 nm from the irradiated surface.

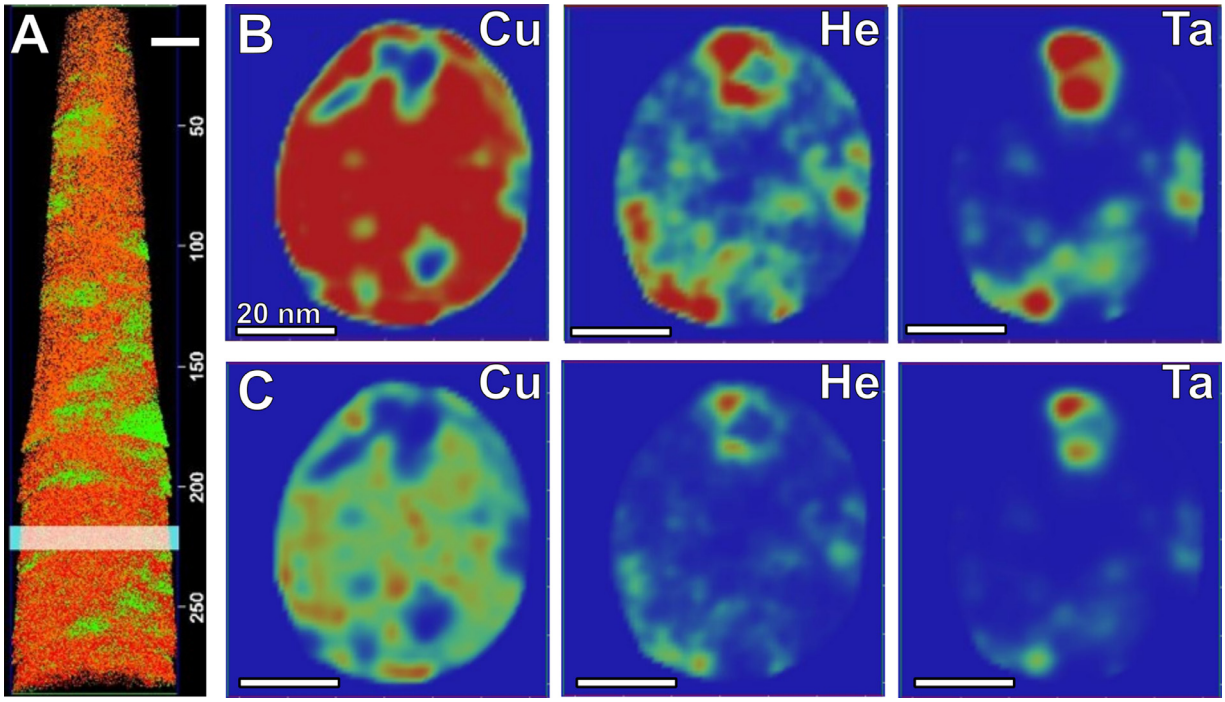

Fig. 4. Helium partitioning to Ta clusters (A) Atom map of an APT specimen prepared from the irradiated surface (to a depth of ~300 nm) for the RT irradiation, where Cu is shown in orange and Ta in green. (B-C) 2-D contour density maps of a 10 nm thick slice taken from the highlighted region in the APT needle of part A showing the distribution of Cu, He, and Ta atoms within that slice at different maximum intensities.

helium profile [25,26]. The bubble density at an irradiated depth of ~450 nm was calculated to be around $1.2 \times 10^{23}/m^3$ which is similar to the nanocluster density on the order of $\sim 6.6 \times 10^{23}/m^3$ [27], further agreeing with the TEM observation where at depths until 400 nm, most of the bubbles were associated with/primarily observed along the Ta nanoclusters. In addition to the swelling resistance, the microstructural stability was exceptional with a minimum grain growth from an average of 50 nm in the as-received state to ~85 nm at a He concentration and dose of 3 at.% and 2.5 dpa respectively at 723 K. This stability of the nanocrystalline microstructure provides additional proof for the stability and effectiveness of the Ta nanoclusters in pinning the GBs at such high helium levels.

To further analyze the effectiveness of these Ta nanoclusters in trapping helium, atom probe analysis was carried out as shown in Fig. 4, which enables mapping of relative atom positions. Fig. 4A shows an APT tip of an RT implanted specimen comprising the top 300 nm from the irradiated surface. A 2-D slice of 10 nm thickness was taken along the z-axis from the APT tip ~225 nm from the irradiated surface as highlighted in Fig. 4A, and their corresponding contour density maps are plotted with two different maximum intensities in Fig.s 4B and C. The 2D contour density maps for Cu, He, and Ta show the overlap of high-density region of He with that of Ta, indicating a preferential partitioning of helium to the nanoclusters. Multiple 2-D slices were analyzed to validate this behavior. Moreover, the iso-concentration surface generated for tantalum and helium (Figure S2) also indicated a vast majority of helium going into tantalum. To put in perspective, the helium concentration in copper matrix and tantalum precipitates were calculated using proxigrams from atom probe data to be ~0.23 and 1.46 at.% helium respectively (Table S1). This high affinity of tantalum to helium reduces the amount of helium available freely to bind with vacancies and form large helium bubbles at the matrix and GBs. Such high binding of helium to tantalum was observed in W-5Ta where the

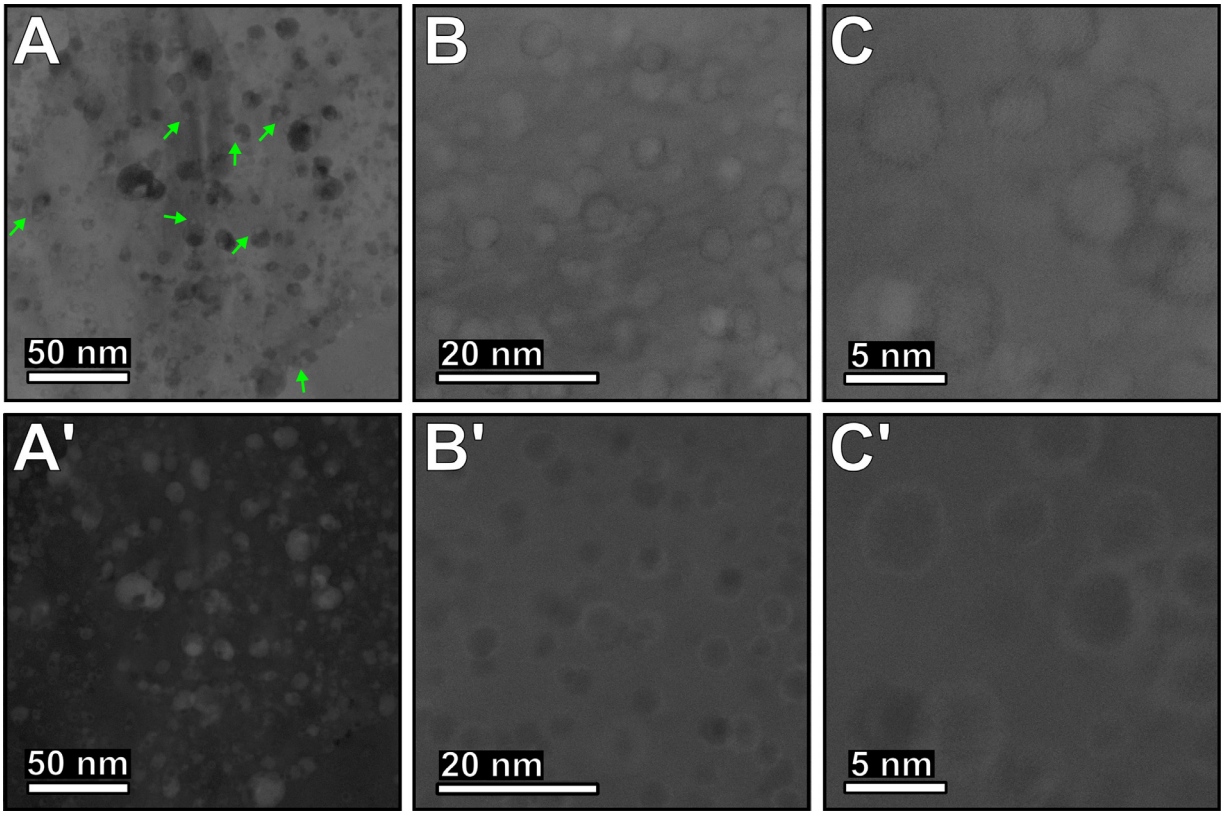

Fig. 5. (A-C) BF STEM images and the corresponding HAADF images (A'-C') of Ta nanoclusters in the specimens irradiated at 723 K showing the presence of Helium bubbles at the (A) interfaces and (B-C) the core of the nanoclusters.

binding energy further increased with the addition of more helium atoms to tantalum [28]. Additionally, the radial distribution function of various elements (Figure S3) with respect to tantalum also confirmed the increased affinity of helium towards tantalum further highlighting that the Ta nanoclusters are the preferential sites for helium segregation and bubble nucleation in the Cu-Ta system.

Immiscible semi-coherent heterophase boundaries have been considered effective sinks for radiation-induced defects due to their high density of misfit dislocation interfaces (MDIs). In fact, comparing the O-lattice theory calculations (in [13]) that correlates the MDI density and the lattice parameter ratio in fcc/bcc interface to the lattice parameter ratio of Ta and Cu (0.91) indicates a high density of areal MDIs at Cu/Ta interface similar to Cu-Nb interfaces, which are considered efficient sinks for radiation-induced defects [4]. The effectiveness of these MDI's in absorbing defects is evident from the TEM observations (e.g., Fig. 5A) and the high critical helium concentration/interface area of ~7.8-9.9 atoms/nm^2 in Cu/Ta compared to other immiscible interfaces like Cu-V or Cu-Mo [4]. Interestingly, high-resolution TEM images of the nanoclusters post-irradiation (Fig. 5(B-C)) reveal a low-density core within the shell of tantalum nanoclusters indicating helium accumulation and bubble nucleation within the tantalum nanoclusters, whose growth is typically limited by the size of the clusters. Earlier works on the chemistry of the nanoclusters indicated that the nanoclusters exhibit a core-shelled structure with the core rich in oxygen and vacancies embedded in the tantalum shell [27]. Such vacancy trapping mechanisms have been reported in oversized solutes and have been proposed as an effective mechanism to suppress void swelling [29]. Thus, in addition to the misfit dislocations in the semi-coherent interfaces of these nanoclusters (Fig. 5A), the defected cores in the core-shell structured nanoclusters provide additional free volume for effective helium trapping and serve as preferred nucleation sites for helium bubbles in Cu-10at.%Ta as seen in Fig. 5(B-C). Overall, this unique combination of attributes of Ta nanoclusters makes them very effective in trapping helium atoms.

In summary, helium irradiation was carried out on NC Cu-10at.%Ta to a peak helium concentration of 4 at.% He at RT and 723 K. The TEM analysis of the cavity distribution shows a large density of bubbles associated with the nanoclusters. This is further confirmed through APT analysis, which indicates a high affinity of helium to tantalum leading to preferential nucleation of helium bubbles at tantalum nanoclusters in Cu-10at.%Ta. In addition to the nanocluster interfaces, the defected cores were also observed to provide additional free volume for helium trapping. Furthermore, low peak swelling of ~0.8% observed at 723 K provides additional validation for the effectiveness of these clusters in sequestering helium bubbles and suppressing swelling.

Declaration of Competing Interest

The authors declare that they have no known competing financial interests or personal relationships that could have appeared to influence the work reported in this paper.

Acknowledgment

Ion irradiation was performed at the Center for Integrated Nanotechnologies (CINT), an Office of Science User Facility operated for the U.S. Department of Energy (DOE) Office of Science. Los Alamos National Laboratory, an affirmative action-equal opportunity employer, is managed by Triad National Security, LLC for the U.S. Department of Energy's NNSA, under contract 89233218CNA000001. S.S. and K. N. S. acknowledge the use of facilities within the LeRoy Eyring Center for Solid State Science at Arizona State University. This work was supported by US Army Research Laboratory under contract W911NF-15-2-0038 and the National Science Foundation

No. 1663287. K.A.D acknowledges A.J Roberts and T. Luckenbaugh for the synthesis of the Cu-Ta powder.

Supplementary materials

Supplementary material associated with this article can be found, in the online version, at doi:10.1016/j.scriptamat.2021.114344.

References

[1] S.J. Zinkle, G.S. Was, Acta Mater. 61 (2013) 735–758.
[2] S.J. Zinkle, J.T. Busby, Mater. Today 12 (2009) 12–19.
[3] A.A. Lucas, Phys. BC 127 (1984) 225–239.
[4] S.-H. Li, J.-T. Li, W.-Z. Han, Materials 12 (2019) 1036.
[5] K. Farrell, Radiat. Eff. 53 (1980) 175–194.
[6] H. Trinkaus, B.. Singh, J. Nucl. Mater. 323 (2003) 229–242.
[7] M.A. Tschopp, F. Gao, L. Yang, K.N. Solanki, J. Appl. Phys. 115 (2014) 033503.
[8] Y. Dai, G.R. Odette, T. Yamamoto, in: Compr. Nucl. Mater, Elsevier, 2012, pp. 141–193.
[9] X. Zhang, K. Hattar, Y. Chen, L. Shao, J. Li, C. Sun, K. Yu, N. Li, M.L. Taheri, H. Wang, J. Wang, M. Nastasi, Prog. Mater. Sci. 96 (2018) 217–321.
[10] O. El-Atwani, J.E. Nathaniel, A.C. Leff, B.R. Muntifering, J.K. Baldwin, K. Hattar, M.L. Taheri, J. Nucl. Mater. 484 (2017) 236–244.
[11] D.T. Hoelzer, C.P. Massey, S.J. Zinkle, D.C. Crawford, K.A. Terrani, J. Nucl. Mater. 529 (2020) 151928.
[12] G.R. Odette, D.T. Hoelzer, JOM 62 (2010) 84–92.
[13] M.J. Demkowicz, A. Misra, A. Caro, Curr. Opin. Solid State Mater. Sci. 16 (2012) 101–108.
[14] W. Han, M.J. Demkowicz, N.A. Mara, E. Fu, S. Sinha, A.D. Rollett, Y. Wang, J.S. Carpenter, I.J. Beyerlein, A. Misra, Adv. Mater. 25 (2013) 6975–6979.
[15] K.Y. Yu, Y. Liu, E.G. Fu, Y.Q. Wang, M.T. Myers, H. Wang, L. Shao, X. Zhang, J. Nucl. Mater. 440 (2013) 310–318.
[16] X. Zhang, E.G. Fu, A. Misra, M.J. Demkowicz, JOM 62 (2010) 75–78.
[17] N. Li, E.G. Fu, H. Wang, J.J. Carter, L. Shao, S.A. Maloy, A. Misra, X. Zhang, J. Nucl. Mater. 389 (2009) 233–238.
[18] N. Li, M.S. Martin, O. Anderoglu, A. Misra, L. Shao, H. Wang, X. Zhang, J. Appl. Phys. 105 (2009) 123522.
[19] K.A. Darling, M. Rajagopalan, M. Komarasamy, M.A. Bhatia, B.C. Hornbuckle, R.S. Mishra, K.N. Solanki, Nature 537 (2016) 378–381.
[20] S.A. Turnage, M. Rajagopalan, K.A. Darling, P. Garg, C. Kale, B.G. Bazehhour, I. Adlakha, B.C. Hornbuckle, C.L. Williams, P. Peralta, K.N. Solanki, Nat. Commun. 9 (2018) 2699.
[21] M. Rajagopalan, K.A. Darling, C. Kale, S.A. Turnage, R.K. Koju, B.C. Hornbuckle, Y. Mishin, K.N. Solanki, Mater. Today 31 (2019) 10–20.
[22] S. Srinivasan, C. Kale, B.C. Hornbuckle, K.A. Darling, M.R. Chancey, E. Hernández-Rivera, Y. Chen, T.R. Koenig, Y.Q. Wang, G.B. Thompson, K.N. Solanki, Acta Mater. 195 (2020) 621–630.
[23] R.E. Stoller, M.B. Toloczko, G.S. Was, A.G. Certain, S. Dwaraknath, F.A. Garner, Nucl. Instrum. Methods Phys. Res. Sect. B Beam Interact. Mater. At. 310 (2013) 75–80.
[24] Standard Practice for Neutron Radiation Damage Simulation by Charged-Particle Irradiation, 96.
[25] Q. Li, C.M. Parish, K.A. Powers, M.K. Miller, J. Nucl. Mater. 445 (2014) 165–174.
[26] E.G. Fu, A. Misra, H. Wang, L. Shao, X. Zhang, J. Nucl. Mater. 407 (2010) 178–188.
[27] B.C. Hornbuckle, T. Rojhirunsakool, M. Rajagopalan, T. Alam, G.P. Purja Pun, R. Banerjee, K.N. Solanki, Y. Mishin, L.J. Kecskes, K.A. Darling, JOM 67 (2015) 2802–2809.
[28] I. Ipatova, G. Greaves, S. Pacheco-Gutiérrez, S.C. Middleburgh, M.J.D. Rushton, E. Jimenez-Melero, J. Nucl. Mater. 550 (2021) 152910.
[29] F.A. Smidt, J.A. Sprague, Scr. Metall. 7 (1973) 495–501.